



Towards Predicting the Onset of Elastic Turbulence in Complex Geometries

Eseosa M. Ekanem¹ · Steffen Berg^{1,2} · Shauvik De³ · Ali Fadili² · Paul Luckham¹

Received: 7 February 2022 / Accepted: 20 April 2022 / Published online: 16 May 2022
© The Author(s) 2022

Abstract

Flow of complex fluids in porous structures is pertinent in many biological and industrial processes. For these applications, elastic turbulence, a viscoelastic instability occurring at low Re —arising from a non-trivial coupling of fluid rheology and flow geometry—is a common and relevant effect because of significant over-proportional increase in pressure drop and spatio-temporal distortion of the flow field. Therefore, significant efforts have been made to predict the onset of elastic turbulence in flow geometries with constrictions. The onset of flow perturbations to fluid streamlines is not adequately captured by Deborah and Weissenberg numbers. The introduction of more complex dimensionless numbers such as the M -criterion, which was meant as a simple and pragmatic method to predict the onset of elastic instabilities as an order-of-magnitude estimate, has been successful for simpler geometries. However, for more complex geometries which are encountered in many relevant applications, sometimes discrepancies between experimental observation and M -criteria prediction have been encountered. So far these discrepancies have been mainly attributed to the emergence from disorder. In this experimental study, we employ a single channel with multiple constrictions at varying distance and aspect ratios. We show that adjacent constrictions can interact via non-laminar flow field instabilities caused by a combination of individual geometry and viscoelastic rheology depending (besides other factors) explicitly on the distance between adjacent constrictions. This provides intuitive insight on a more conceptual level why the M -criteria predictions are not more precise. Our findings suggest that coupling of rheological effects and fluid geometry is more complex and implicit and controlled by more length scales than are currently employed. For translating bulk fluid, rheology determined by classical rheometry into the effective behaviour in complex porous geometries requires consideration of more than only one repeat element. Our findings open the path towards more accurate prediction of the onset of elastic turbulence, which many applications will benefit.

Article Highlights

- **We demonstrate that adjacent constrictions “interact” via the non-laminar flow fields caused by individual constrictions, implying that the coupling of rheological effects and fluid geometry is more complex and implicit.**

- **The concept of characterizing fluid rheology independent of flow geometry and later coupling back to the geometry of interest via dimensionless numbers may fall short of relevant length scales, such as the separation of constrictions which control the overlap of flow fields.**
- **By providing direct experimental evidence illustrating the cause of the shortcoming of the status-quo, the expected impact of this work is to challenge and augment existing concepts that will ultimately lead to the correct prediction of the onset of elastic turbulence.**

Keywords Multiple microchannel · Microfluidics · Viscoelasticity · Polymers

1 Introduction

In the last few decades, there have been significant efforts to understand the flow behaviour of complex fluids in intricate geometries more relevant to applications in a wide variety of industrial processes such as moulding, extrusion, coating, spraying, flow of polymer melts and aqueous solutions, lubricant grease for machine bearings, pharmaceutical applications (Hossein et al. 2016; Mahmoodi et al. 2021) and in medicine, where the non-Newtonian rheology of blood is important and a very relevant factor in the development of arterial stenosis where multiple local arterial narrowing can evolve due to the unsteady blood flow caused by the instability, which leads, in the worst case, to potentially life-threatening biomedical conditions in the cardio-vascular system (GAO et al. 2009; Li et al. 2014; Mustapha et al. 2008; Rabby et al. 2014). Another important class of application is in the recovery and/or storage of fluids in the sub-surface, where the impact of the complex rheology can be significant (Clarke et al. 2016; Parsa et al. 2020; Skauge et al. 2018; Wever et al. 2011; Zamani et al. 2015). All these applications combine a non-Newtonian fluid rheology with complex geometries to some degree, therefore, understanding those interactions and their effects on the overall process is key for the improvement and the determination of the optimal application window.

The conventional method used in investigating the interplay between the fluid flow rheology (assumed to be independent of the container) and geometry is to reduce the level of complexity and decompose these applications into the flow geometry and the properties of the complex fluid, which is characterized by independent measurements. The bulk rheology of the fluid is typically measured with standard methods such as a rotational rheometer independent of the specific geometry in the application. The effective in situ behaviour of the fluid flowing inside the complex geometry is then obtained by coupling the bulk rheology with the local geometry and fluid velocity using concepts such as shear rate and extensional rate. The assumption is that a universal in situ behaviour can be described by using scaling relationships or dimensionless groups, where similar behaviours can be found for different geometries and flow rates but identical shear and extensional rates.

The fluids most relevant for technical applications often exhibit in addition to the viscous response also an elastic component (Sadeghi et al. 2012). The complication with these so-called viscoelastic fluids is that the in situ behaviour of these fluids in the complex flow geometry can show additional effects compared to what is observed in the corresponding bulk rheology measurements. Elastic turbulence, which is an important feature for many of the relevant applications, is an instability caused by the interplay of the fluid's

elasticity occurring within specific flow geometries such as channels with constrictions such as in arterial stenosis. The term “elastic turbulence” has been used in analogy to Kolmogorov’s turbulence, but it occurs already at much lower Reynold’s numbers (van Buel and Stark 2020; Choueiri et al. 2021; De et al. 2017a; Groisman and Steinberg 2000; Jun and Steinberg 2011; Kawale et al. 2017; Samanta et al. 2013; Steinberg 2021). One of the consequences of elastic turbulence is the significant and over-proportional increase in pressure drop (De et al. 2017a). For Newtonian fluids, the pressure drop increases proportional with the increase in flow rate (shear rate). For the complex fluids of interest, such as polymer solutions and blood which exhibit mostly shear-thinning viscous behaviour (Qi and Shaqfeh 2018), expectations are for the pressure drop to decrease less rapidly than Newtonian fluids, which is one of the reasons why polymer solutions are selected for improved oil recovery processes. However, elastic turbulence causes the pressure drop to increase in a strongly over-proportional manner which leads to far reaching consequences, for instance the risk of heart attack in arterial stenosis and overpressure of the sub-surface during fluid storage/recovery. In cases where polymer solutions are present, elastic turbulence leads to repeated and rapid stretching and collapse sequences of the polymer chain (Varshney and Steinberg 2019) which may damage high molecular weight polymers resulting in an undesired strong reduction in viscosity (De et al. 2017a; Garreppally et al. 2020).

Due to its relevance, many attempts have been made to parameterize the in situ effective rheology and predict the effective pressure drop of a viscoelastic fluid flowing in channels with constrictions or porous materials. Several scaling and dimensionless groups such as shear or extensional rate, Weissenberg number (Wi), and Deborah number (De) have been employed to understand the onset of this elastic turbulence (van Buel and Stark 2020; Walkama et al. 2019). Most of these parameters have identified transitions in flow regimes from steady to unsteady behaviour and even time-dependent flow behaviour (Zilz et al. 2012). However, when probing in detail the flow behaviour in more complex geometries having varying lengths between constrictions and varying aspect ratios, capturing the onset of turbulence is not as simple as the use of the dimensionless parameters mentioned above and attempts to predict the onset have been largely unsuccessful.

This is a long-standing problem. It has always been clear that De and Wi numbers capture only the end members of the more general case. We find that the De and Wi should coincide in situations where only one length scale determines the dynamics of the problem. When multiple length scales are critical to determining the problem, a geometric factor can relate both dimensionless numbers. Hence, McKinley and co-authors introduced the M criteria which combine both De and Wi , to capture the in situ effective behaviour by only one scaling group (Alves and Poole 2007; Browne et al. 2020; McKinley et al. 1996; Pakdel and McKinley 1996; Zilz et al. 2012), which is intended as a simple and pragmatic order-of-magnitude estimate for the onset of viscoelastic instabilities.

Most of the literature has focused on geometries with one single constriction (Ekanem et al. 2020; Haward et al. 2019; Hopkins et al. 2021; Raihan et al. 2021; Zhao et al. 2016) to conceptualize the fundamental fluid rheology – geometry relationship. In such geometries, the M criteria have been reasonably successful as a dimensionless parameter that predicts the onset of distortion to the fluid streamlines from laminar behaviour where the surrounding is laminar and the instability initiates at the single constriction. However, it has not been successful either in conceptualizing the behaviour in more complex geometries (Browne et al. 2020; Cruz et al. 2014; Haward 2016; Haward et al. 2012; Sousa et al. 2015) with multiple or repeated constrictions, such as found in porous media (McKinley et al. 1996) and also in applications such as arterial stenosis where blood (which is a viscoelastic fluid) flow encounters irregular arterial surfaces and asymmetric lesions at

multiple locations (Khodaparast et al. 2014; Mustapha et al. 2008; Qin et al. 2019; Rabby et al. 2014; Zografos et al. 2020). The established literature on the topic mainly focuses on either *single* repeat units or structures with *many* repeat units which start with regular patterns and an increasing degree of randomness is introduced. The deviations of the observed onset of elastic turbulence from the prediction by the M-criteria are then largely explained by an emergence as a consequence of disorder (Cruz et al. 2014; Haward 2016; Haward et al. 2012; Sousa et al. 2015).

However, that systematics leaves a gap as to how the effective in situ behaviour becomes more than the sum of its individual parts. By addressing the problem with a sequence of constrictions at varying separation distances, it becomes evident why De , Wi and M do not provide an entirely sufficient description of the instability, including its onset. The cause is a more complex interaction between adjacent constrictions which couple via the flow field resulting from a combination of respective local geometry at the constriction and fluid rheology. Depending on the distance between adjacent throats in the flow geometry, the flow field turbulence, which is elastic in nature, moves upstream (Qin et al. 2019) and may interact with the preceding throat, depending on different conditions that relate to the interaction between the fluid velocity and the porous media geometry. By using a flow geometry consisting of a single channel, with a sequence of constrictions with varying distance between adjacent constrictions and varying aspect ratio, which is the elementary geometry typically considered for arterial stenosis (Khodaparast et al. 2014; Mustapha et al. 2008; Qin et al. 2019; Rabby et al. 2014; Zografos et al. 2020), we can show in an elementary way the varying interaction between subsequent throats via the (unstable) flow field, where the magnitude of the interaction depends on the degree of flow field instability, i.e. has an onset which coincides when the unstable flow field reaches the adjacent *upstream* pore throat. This means that for a given bulk fluid rheology, in a porous medium, the effective pressure drop is also influenced by the specifics of the porous medium in terms of distance between constrictions and size of the constrictions which introduces another length scale into the problem.

2 Materials and Methods

2.1 Polymer Solution Preparation

Hydrolyzed polyacrylamide (HPAM), an anionic polyelectrolyte, was used as the viscoelastic fluid because it is a commonly used and well-studied model system and has practical relevance for a range of applications (Garrepally et al. 2020; Jun and Steinberg 2011; Yao et al. 2019).

It is comprised of both acrylamide monomer and 30% acrylic acid monomer and was obtained from SNF Floerger. It has a molecular weight range between 18 and 20 MDa. The HPAM solution was prepared in the presence of 0.5% NaCl and purchased from Sigma-Aldrich. The solution was also prepared in de-ionized (DI) water with a protective package (containing 15% isopropanol, 7.5% thiourea, and 77.5% water) added to minimize polymer degradation, such that the final concentration of isopropanol is 20% of the polymer concentration. Preparation of the solution was carried out on a magnetic stirrer with a magnetic stirring rod placed inside the solution at a high speed for the first 10 min and reduced to medium speed for 48 h to ensure proper dissolution and hydration of the

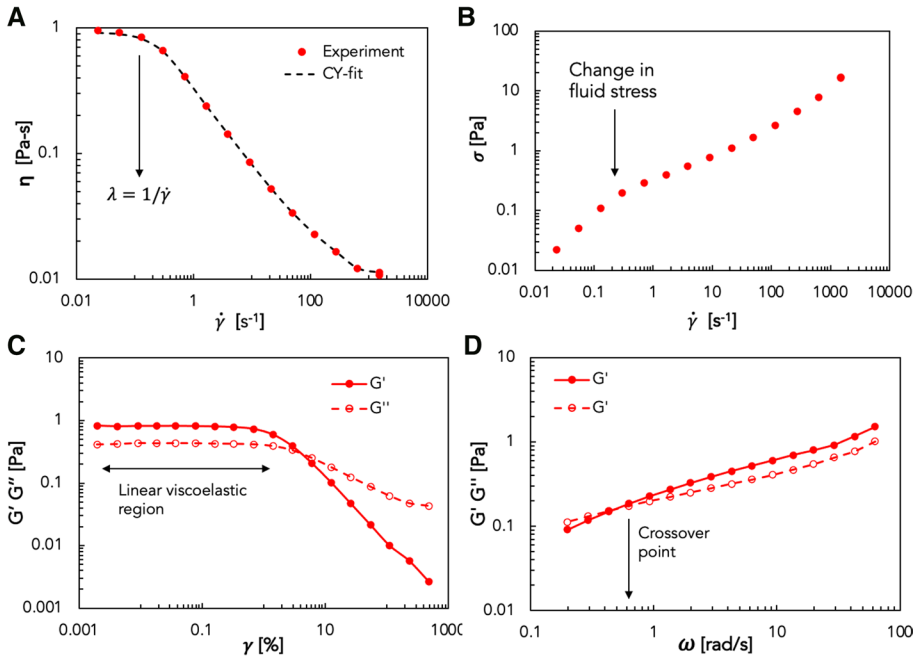


Fig. 1 Bulk characterization of hydrolyzed polyacrylamide (HPAM). (A) Shear viscosity versus shear rate with a Carreau Yasuda fit (B) Shear stress as a function of the shear rate (C) Amplitude sweep of G' G'' versus strain, showing the linear viscoelastic region (D) Frequency sweep of G' G'' versus the angular velocity at a strain of 0.1

individual polymer molecules. (De et al. 2018a, b). Figure 1 shows the bulk characterisation of HPAM using standard rheometry.

2.2 Microfluidic Experiment and Visualization

Experiments were carried out in two microfluidic channels of length 37.2 mm long, comprising four constrictions represented by throats and five channel bodies represented by pores. The channels were designed in-house and fabricated by Dolomite, United Kingdom. The first channel has a throat width of 0.4 mm, and the second channel 0.2 mm. Image analysis was performed for both channels and only in the first three throats with its associated pore bodies as denoted with a red line in Fig. 2. HPAM and Newtonian fluid (Gly: water) as described in Table 1 is injected into the channel at different flow rates from left to right, such that an average velocity $U_{av} = Q/h_w$ is imposed. Channel 1 has a contraction ratio ($CR = \text{width of pore}/\text{width of constriction} = w_u/w_c$) of 5, and channel 2 has a $CR = 10$. Exact dimensions are listed in Table 2. The geometry is inspired by previous work [29] which provided guidance for which geometry and dimensions the onset of elastic turbulence can be expected to occur for a given fluid system and typical flow rates that make imaging at sufficient frame rates feasible to capture the flow field.

The dimensionless M number is utilized in place of the flow rate Q . The critical M denoted as M_{crit} (Eq. 2) occurs at the onset of an infinitesimal perturbation to the fluid streamline. We obtain different M numbers from 2 to 18 in both channels as the flow rate

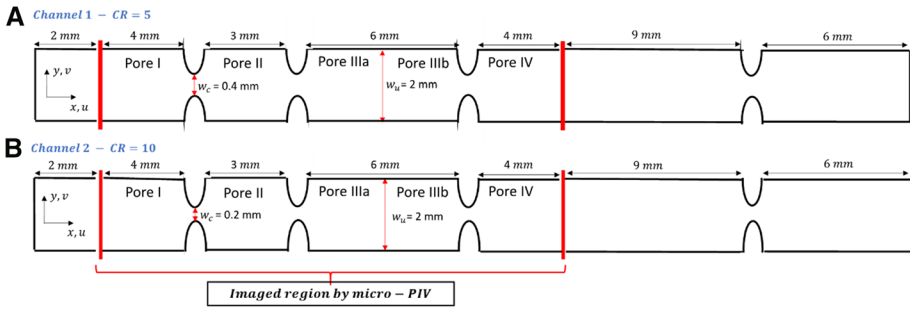


Fig. 2 Microfluidic channel geometry investigated for polymer solution flow by microparticle image velocimetry technique **A** represents channel 1 with a contraction size of 0.4 mm and an aspect ratio (AR) of 5. **B** Represents channel 2 with a contraction size of 0.2 mm and an aspect ratio (AR) of 10. The imaged region considered is marked with red lines

Table 1 Description and summary of the properties of each solution

Solution	Polymer Conc. (ppm)	Salt	C _{salt} (%)	η ₀ (Pas)	Re range	λ (s)	CY fitting parameters				
							η ₀ (Pa s)	η _α (Pa s)	n	a	λ _{CY} (s)
Gly.: water (84% Gly. & 16% water)	–	–	–	0.06	10 ² –10	–	–	–	–	–	–
HPAM	2000	NaCl	0.5	0.59	10 ³ –10 ¹	4	0.82	0.01	0.04	1.01	0.07

Table 2 Characteristic dimensions of the micro-channels used in this work

Geometry	Channel width, w _u (μm)	Constriction width, w _c (μm)	Aspect ratio (AR = w _u /w _c)	Channel height, h (μm)
Channel 1	2000	400	5	200
Channel 2	2000	200	10	200

of HPAM is increased. The flow behaviour of both channels is shown, where CR = 5 is represented by M = 2, 6, 9 and 13, while CR = 10 represents M = 4, 8, 14 and 18. For imaging, the flow cell was divided in two separate field of views, namely pore I-IIIa and the pore IIIb and IV, which were afterwards connected (which is still visible as a small discontinuity, which has no influence on the conclusions).

Fluid flow visualizations were carried out using a micro-particle image velocimetry (μ-PIV) technique. The polymer solution was seeded with fluorescent 2.0 μm polystyrene microspheres obtained from microParticles GmbH. The particle concentration was 0.5% w/v. The μ-PIV set-up consisted of an inverted microscope (Leica DMi8), comprising an objective lens of 2.5× magnification (Leica HC PL Fluotar 2.5×/0.07 numerical aperture objective) and a Thorlabs plano-convex round cylindrical lens (f = 250 mm) enclosed in a 2.5× camera adapter (Leica 10,441,675).

The microchannel was first cleaned with an Aquet cleaning solution, using a 10 ml gas tight Hamilton syringe. Afterwards, HPAM-Na was injected into the microchannel with the

same syringe for 5 min to ensure a steady flow, before flow field visualization of HPAM-Na began. The fluid effluent was collected in a vial with a long tubing connected to the microchannel outlet and free from any obstruction, to prevent downstream perturbations and backflow.

During flow visualization, images were acquired at a constant x–y plane, located at the midpoint of the z-axis direction. The centre plane of the channel was determined by first observing the top and bottom surface, with the help of supplier markings, then averaging the distance between both surfaces to get the mid-plane. In order to avoid long streak images during flow visualization, the exposure time was set at 550 μs and then reduced continuously as the flow rate increased, ensuring that all particle displacement between successive frames were optimal. The velocity distribution in each frame was obtained, by carrying out a cross-correlation analysis with the particle displacement and time between two successive frames. This correlation analysis was processed using the PIVLAB open-source tool on MATLAB.

2.3 Dimensionless Numbers

The polymer solution is injected into the microchannel at a controlled volumetric flow rate, using two syringe pumps, obtained from Fischer Scientific, UK. The upstream average velocity in the channel is $U_{av} = \frac{Q}{hw_u}$ where h is the channel height and w_u is the channel upstream width. The Reynold's number, Re , is defined in Eq. 1, based on the average velocity, u_c

$$Re = \frac{\rho u_c d_h}{\eta_0} = \frac{2\rho Q}{\eta_0(h + w_c)} \quad (1)$$

where the density of the polymer solution is ρ , the hydraulic diameter, $d_h = \frac{2w_c h}{(w_c + h)}$, and the velocity at the contraction is u_c . We have expressed the viscosity, η_0 , as the zero-shear rate viscosity because choosing either the zero-shear rate viscosity, infinite-shear rate viscosity or the local-shear rate-dependent viscosity, will have negligible effect on the magnitude of Re , for all flow conditions.

Due to the instabilities of viscoelastic solutions, which have been studied and observed in so many situations, especially with microchannels (Browne et al. 2020; Gutiérrez et al. 2020; Hopkins et al. 2021; Howe et al. 2015; Mitchell et al. 2016), a dimensionless M criteria, for the onset of purely elastic flow instabilities, were proposed as a pragmatic and simple concept by Pakdel & Mckinley (Mckinley et al. 1996; Pakdel and McKinley 1996). This dimensionless M criteria, in Eq. 2, considers both the elastic stresses and the curvature of the fluid streamlines, as elastic instabilities emerge from the coupling of both quantities causing a tension in the fluid streamline.

$$\left[\frac{\lambda u}{\mathfrak{R}} \frac{\tau_{11}}{\eta_0 \dot{\gamma}} \right]^{\frac{1}{2}} \geq M_{crit} \quad (2)$$

where the first term $\frac{\lambda u}{\mathfrak{R}}$, relates to the Deborah number, De , with λu , representing the length scale to which perturbations to the base viscoelastic stress and velocity fields relax. Here, $1/\mathfrak{R}$ is the radius of curvature and a dimensionless measure of the relative distance over which the disturbances are advected compared to the local curvature of the flow. τ_{11} represents the stress, and $\dot{\gamma}$ represents the shear rate. Since our geometry has a hyperbolic contraction, we use Eq. 3, to estimate the radius of curvature at the contraction.

$$\mathfrak{R} = \frac{w_p - w_c}{2} = \frac{w_c}{2}(CR - 1) \quad (3)$$

The second term in Eq. 2 is representative of the Weissenberg number, which is the ratio of elastic stresses to viscous stresses. Therefore, we can write the dimensionless M criteria in relation to Deborah and Weissenberg number as follows:

$$M = \sqrt{DeWi} \quad (4)$$

The Deborah number is $De = \frac{\lambda u}{\mathfrak{R}}$ and the Weissenberg number is $Wi = \frac{\tau_{11}}{\eta_0 \dot{\gamma}}$. Defining the Deborah number for a fluid that is both viscoelastic and shear-thinning can be more difficult. Here, we use the zero-shear rate viscosity limit for consistency. Note that, there are also more advanced definitions with a modified dimensionless number that also considers the shear-thinning (Xie et al. 2022).

The stress, τ_{11} , in Eq. 2 is represented by the normal stress N_1 and obtained using the equation $\frac{2F}{\pi R^2}$ where F is the normal force obtained during rotational experiment, while using a cone and plate geometry (angle = 2°) and R is the radius of the plate geometry.

Calculating and inputting all the terms in Eq. 2, with M_{crit} being the onset for purely elastic instability in the microchannel, we obtain M values, that range $\approx 2 - 18$, for the experiments carried out in this work.

3 Results and Discussion

The core of the experiment is a microfluidic device that consists of single channels with multiple constrictions at different distance. For the constrictions, two different aspect ratios AR (ratio of upstream width and constriction width) were considered. For details, we refer to Fig. 2. In Fig. 3, we show the velocity field as obtained from particle image velocimetry, for a viscoelastic aqueous solution of high-molecular weight polyacrylamide (for details see Table 1). The injection rate is varied to cover flow regimes from laminar to elastic turbulence. Note that, Fig. 3 is a combination of the two aspect ratios (CR = 5 and CR = 10) studied. The different injection rates and aspect ratios result in an increasing Pake-del–Mckinley M criterion.

We observe that for $M=2$, the flow field is mainly laminar. For $4 \leq M \leq 6$, the flow field remains laminar but not fully symmetric. We observe that at $M=4$, the first disturbance to the fluid streamline occurs with a localized distortion at each individual constriction (essentially an unsteady eddy at the upstream location of each pore throat) with an evolution of a streamwise vortex (Browne et al. 2020) suggesting that $M_{crit}=4$. We also find that as the velocity proceeds to higher M number, the flow perturbations do not remain localized in each pore and constriction of both channels. These perturbations and vorticities grow in length as shown in Fig. 3 causing interactions between pores depending on the pore length and are characterized by flow instabilities or turbulence that are elastic in nature and usually termed “elastic turbulence” (De et al. 2017b; Ekanem et al. 2020; Groisman and Steinberg 2004). The vortex-like structures that were previously constrained to the constriction at lower M values begin to form bridges between adjacent constrictions at $M=8$ for the smallest separations (pores I and II).

At sufficiently large M ($M=8$), the perturbed flow develops into larger circulating vortices in pore II, the smallest pore body, and is advected upstream of the preceding constriction (Qin et al. 2019). In the largest pore body represented by pore III, this behaviour of

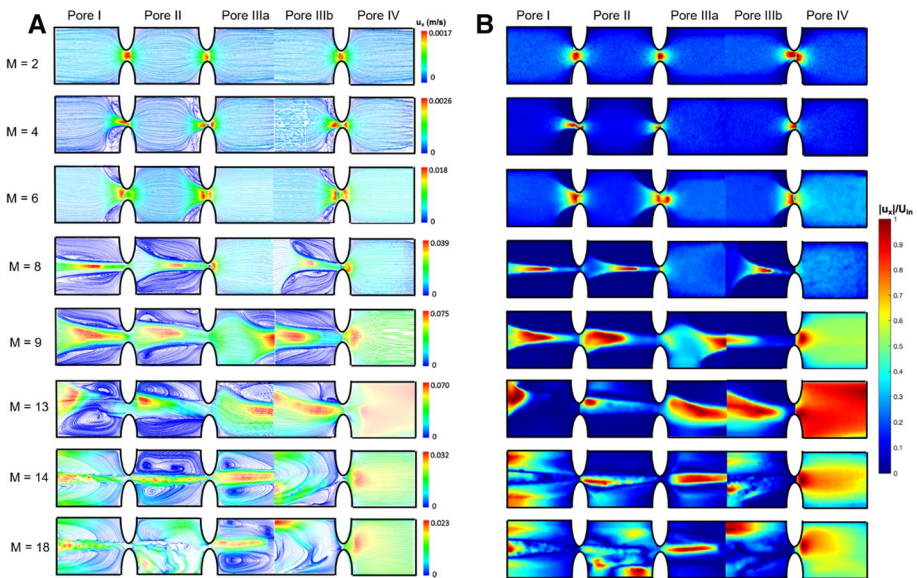


Fig. 3 **A** Velocity streamlines of the flow fields. **B** Normalized velocity ($|u_x|/U_{in}$, where U_{in} is the inlet velocity) for each pore body from pore I – pore IV for all M numbers. $|u_x|$ is the velocity of the fluid within the flow domain in each channel. Flow instability increases with M number with the overlapping flow field beginning at $M=8$. The overlapping flow field is characterized by circulating and unstable flow fields which fill the entire pore body upstream and downstream of each pore leading to a complex non-local effect

overlapping flow fields is observed at $M=13$ supporting the strong relationship between flow rate and distance between connecting constrictions. This overlapping flow field continues more strongly as the M increases. For increasing M, we observe the developing viscoelastic instability that propagates progressively upstream (Qin et al. 2019) and begin bridging between the closer spaced constrictions. At $M > 13$, we observe an increase in vortex structures having different sizes with a reduced velocity of the fluid streamlines within the pores, which help to keep the fluid momentum balanced. At this point, the flow fields which are overlapping transition towards a non-local effect (Jun and Steinberg 2011). The change from the non-overlapping flow field below $M=8$ to an overlapping flow field is representative of the complex flow behaviour from a local to a non-local effect. Because of this transition to an overlapping flow field, the separation distances between the constrictions become relevant, i.e. an additional length scale is involved which is not captured by the current dimensionless parameters (De, Wi, M). In the past, this aspect has been difficult to observe and determine in the more complex geometries, or pore structures that have been previously studied, because the channelling of flow paths at high velocities is mostly observed and dependent on the local order–disorder scheme. However, the systematic variation in separation distances and the visualization of the associated flow fields show that the flow field instability overlapping to the next upstream constriction provides a coupling that marks the onset of a localized to a non-local, globally unstable flow pattern. These observations are clearly shown in the movies provided in the supplemental material (S1 – S8) for all M numbers. From the spatial–temporal patterns of the fluid vortices at increasing velocity, we infer that the interplay between the viscoelastic rheology and separation distance between constrictions controls the degree of elastic turbulence and flow field overlap.

The M criteria have been commonly regarded as a measure for the onset of flow field perturbation (Haward et al. 2016; Mckinley et al. 1996). However, variations in the onset of elastic instabilities are observed for different magnitude of M depending on the exact geometry (Browne et al. 2020). While keeping in mind that M has been established as a practical measure with order of magnitude accuracy, the question arises as to why a prediction is not more precise. A leading idea is that there might be missing parameters or effects. Our experiments confirm that view, but also provide an intuitive explanation.

In our geometry, we observe that the systematically increasing separation distances has an influence on the onset of elastic turbulence which can be intuitively related to the coincidence with the overlap of the flow field between constrictions. However, the changing lengths between constrictions is not considered in De or Wi and consequently also not in M .

In order to support this rather intuitive insight that neither De , Wi or M consider the effect of separation distance of pores and the flow field overlap, in the following analysis, we provide a more quantitative description through the coefficient of variation (CoV), shown in Fig. 4. The CoV is a statistical analysis of the temporal flow field variations determined from the standard deviation divided by the mean of u_x along the centre line of the observation region at $y=0$. The CoV is determined using u_x instead of u_y because u_x samples the entire parameter space in an efficient way. Although, most of the distortions to the flow field are observed in u_y , u_x accounts for the upstream and downstream perturbations, averages these distortions over the entire length of the channel and accounts for a single position in u_y making u_x a more efficient analysis. For comparison, to put the CoV for the HPAM solution into perspective, we also plot the CoV for a Newtonian fluid (Gly: water) where the CoV is independent.

If a parameter such as De , Wi or M was truly the non-dimensional parameter describing the effective behaviour of elastic turbulence, then CoV for different separation of constrictions and different AR should all collapse on the same curve. A collapse for $M < 8$ is observed for both aspect ratios because the flow fields are non-overlapping. However, as the M number increases beyond 8 (i.e. beyond the onset of elastic turbulence), a clear deviation in the CoV for the two different AR is observed for the pores with the shortest separation distance between adjacent constrictions while for pore IIIa where the separation distance to the next downstream constriction is largest (keeping in mind that the instability propagates upstream), still a full collapse of the CoV vs. M is observed (Fig. 4C). Pore IIIb (Fig. 4D) is an in-between situation, and pore IV (Fig. 4E) is at the very end without a constriction further downstream. In other words, the non-collapsing CoV vs. M for exactly the situations where the flow fields start overlapping is a very strong indication for the separation distances being an additional relevant parameter so far not considered in M , De and Wi . The phenomenon could be even more complex because the overlap in flow fields makes the phenomenon essentially non-local. The quantification via CoV confirms our previous observations in Fig. 3.

While Fig. 3 provides only specific snapshots in time, we use a space–time plot shown in Fig. 5 to visualize the impact of flow field overlap in a spatio-temporal way. In that way we can clearly show that the flow regime is impacted by the separation distance between pore throats.

We select two regions: pore II and IIIa which differ in the most significant degree in terms of flow field overlap. In the space–time plot, the u_x velocities at $y=0$ are plotted in space over the entire time of the experiments, such that the u_x velocities observed in each

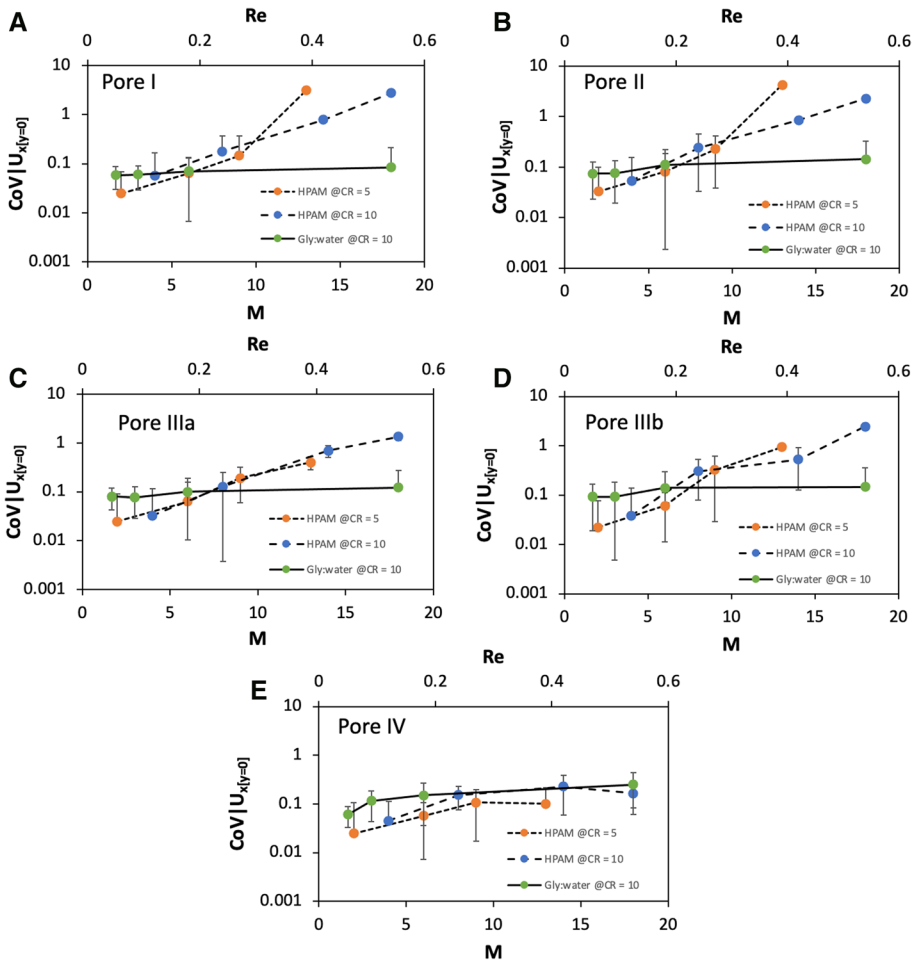


Fig. 4 The coefficient of variation (CoV) of $u_x|_{y=0}$ is plotted as a function of the M number in each pore body for HPAM at CR=5 and CR=10 and for the Newtonian fluid, Gly: water at CR=10. $u_x|_{y=0}$ represents the x-velocity at the centre line of the flow domain where $y=0$. The coefficient of variation (CoV) is the standard deviation divided by the mean of the velocity

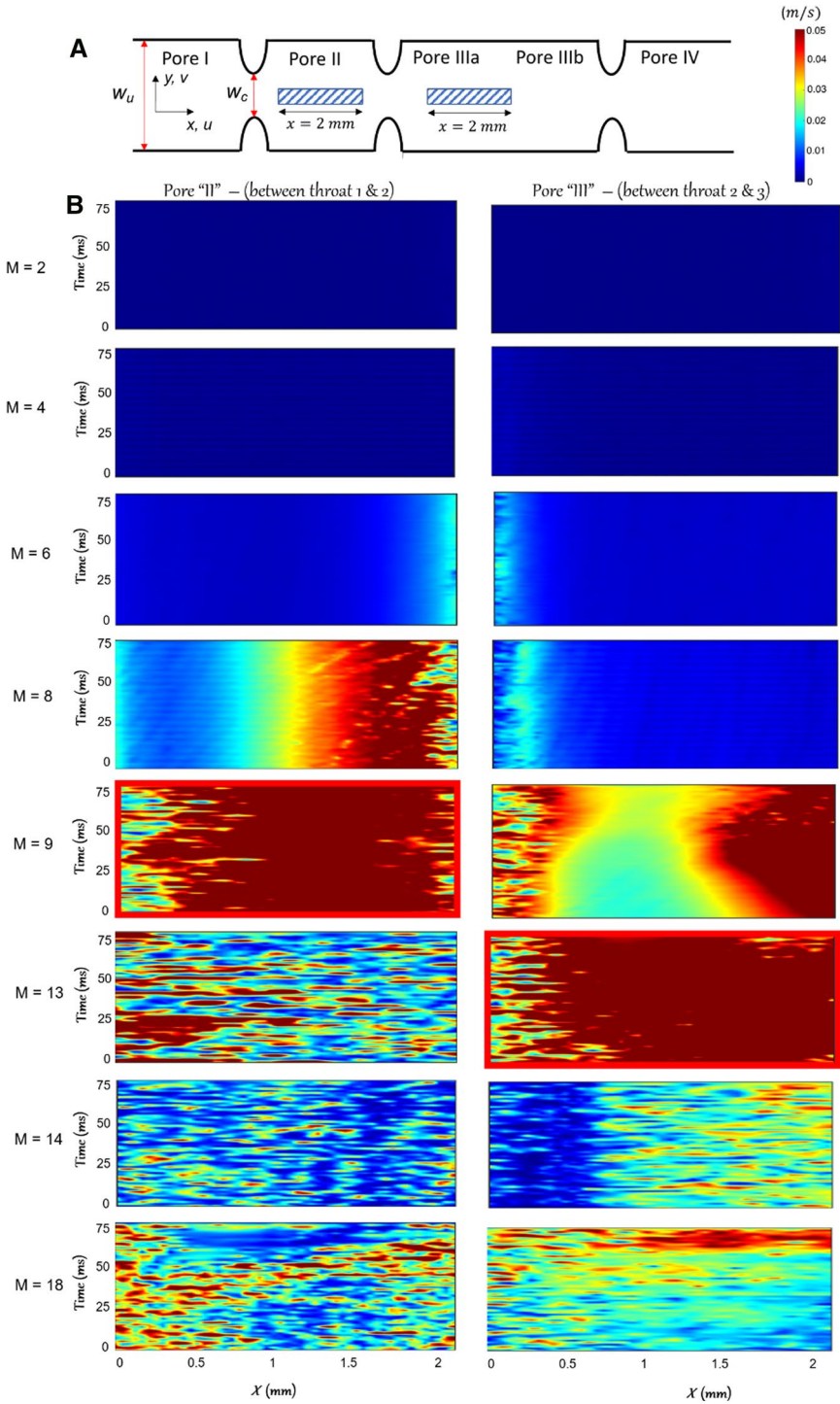
time frame are plotted against the specified space represented. This is shown for all M numbers in pores II, and III. Likewise, below $M=8$, the spatial temporal plot is denoted by a blue colour indicating low velocities and minimal perturbations to the flow field. For $M>8$, there is an interplay between fast flowing and slow flowing velocities that result in flow fluctuations and elastic turbulence. Taking pore II and pore III into consideration because pore II represents a short pore length and pore III, a longer pore length that is double the size of pore II, we observe that the unstable flow field which begins to overlap characterized by an elastic turbulence in pore II begins at $M=8$, but more prominent at $M=9$. However, due to doubling of the pore length in pore III, the overlapping flow fields

Fig. 5 (A) the channel showing marked regions in pores II and III where space–time plots were plotted in ► B. (B) space–time plots for pore II and III for all M numbers, representing channel 1 with $CR=5$ and channel 2 with $CR=10$. The space–time plot represents the centre line velocity, $u_x|_{y=0}$, of the 2 mm marked space in pores II and III plotted over the entire time of the experiment of 0.15 s. Results are indicative of the flow fluctuations and overlapping flow field in each pore. $M=9$ and $M=13$ for pore II and pore III and outlined in red indicating the start of an overlapping flow field

begin at $M=13$. Interestingly, we find similar spatial–temporal flow behaviour for $M=9$ and $M=13$ in pore II and pore III, respectively [see Fig. 5]. As this turbulence continues to propagate upstream of each throat, a new length scale is formed which becomes dependent on the existence of a fully developed elastic turbulence. These results are suggestive of a strong interplay between the fluid flow rate and the nature of the order–disorder porous media geometry, such that while the distance between the contraction in a channel is valid at low flows where perturbations are small, this distance become invalid when a full-scale perturbation to the flow field occurs.

To further support the hypothesis that the moment when flow fields between adjacent pores overlap mark a distinct behaviour and consequently separation distances between constrictions become a relevant system parameter, we consider another, dynamic length scale, the vortex length l_v (Browne et al. 2020). The dimensionless vortex length L is a characteristic length that represents the length of the vortex formed as the fluid streamlines become perturbed in relation to the width of the channel, w_u (i.e. $L=l_v/w_u$). L is determined for all M numbers and in pores I, II, and III representing the pores upstream of each throat. The dimensionless vortex length plotted against the M numbers (Browne et al. 2020) for all three pores mentioned shows a collapse of all curves. There is an increase in L as M increases from $M=4$, where perturbations to the fluid streamline begin until $M=8/9$ where the curve begins to flatten out as shown in Fig. 6. This further indicates that there is a dynamic length scale which is changing until the flow fields begin to overlap and a fully developed instability occurs which obscures that dynamic length scale.

One pertinent question that has been discussed for decades is when the actual elastic turbulence begins, how does it relate to the rheological macroscopic behaviour as in the apparent shear thickening observed, and most importantly, how can it be defined by a scaling group or dimensionless group? We observe from recent work in single contraction channels that the apparent shear thickening rheology does relate to the start of an elastic turbulence and when the unstable flow field upstream of the throat or contraction becomes fully developed. This may not be the case for the multiple contraction channels used in this work as our results show that the turbulence may relate to the onset of the fluid streamline perturbation, when the overlap of the flow fields within the pore begins, or when the fully developed instability is seen as in $M=14$ in Fig. 3. In such single contraction channels, a single dimensionless parameter was used to identify the changes in the flow behaviour. However, with the micro-channels used in this work, a more complex dimensionless parameter or number, may be required to identify the changing flow fields because multiple geometric length scales will have to be considered to determine the true onset of the elastic turbulence.



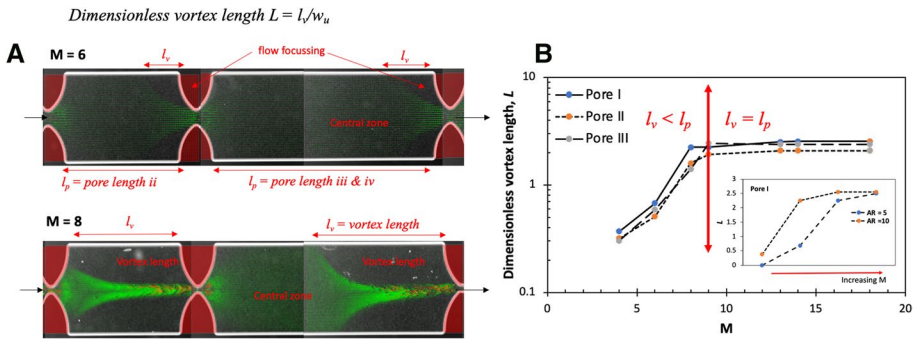


Fig. 6 **A** Shows the image of the velocity vector flowing in the channel with symbols describing the dimensionless vortex length L . Here, L is the ratio of the vortex length l_v to the upstream channel width w_u . The vortex length is an average of five different frames and l_p is the length of each pore. **BA** dimensionless vortex length L is plotted against the M number (Browne et al. 2020) for pores I, II, and III, which represent the pores upstream of each contraction. There is a collapse of all three curves with a transition from $l_v < l_p$ to $l_v = l_p$ at $M=8$, indicating where the flow fields begin to overlap. Insert plot shows that as the AR increases, L increases reaching a plateau and filling up the pore body faster

4 Conclusion

In summary, we have provided intuitive insight into the onset and evolution of elastic turbulence in complex geometries and geometries with multiple constrictions. By imaging the flow field of a non-Newtonian viscoelastic solution in a microfluidic complex geometry consisting of multiple constrictions with varying lengths between constrictions and varying the aspect ratio, we can relate the onset of elastic turbulence and subsequent evolution with the fact that flow fields between adjacent constrictions overlap.

We studied the velocity flow fields and streamlines with increasing M parameter using the micro-particle image velocimetry technique. The M parameter identified the $M_{crit} = 4$ for the onset of perturbations to the fluid streamline and $M=8$ as the onset of an overlapping flow fields.

The covariance of the flow field provided a means of characterization of the different regime and was useful in identifying clearly the separation between successive constrictions as an extra flow parameter. In our geometry, flow fields between adjacent constrictions begin to overlap at $M=8$, which at increasing M developed into a full instability (Browne and Datta 2021).

However, for different geometries (constriction aspect ratios), the streamwise covariance of the flow field does not collapse for De , Wi or M . The reason is that these parameters do not consider the separation distance between constrictions which is evidently relevant.

We show that perturbations to the fluid behaviour which transform towards fully developed turbulence begins from a localized phenomenon, that is characterized by flow disturbances around the constriction of the microchannel and later transforms to a non-localized phenomenon, where the flow turbulence is infinite and fully developed reaching the total length of the pore body repeat unit distance. We further argue that these dimensionless parameters that have been used for over decades may not be the appropriate parameters to define the onset of the elastic turbulence in these geometries because of the unique and dynamic length scale formed by the flow fields as the velocity increases.

Our findings suggest that a criteria describing the onset of elastic turbulence would benefit from consideration of streamwise length scales of the confining geometry such as distances between adjacent pore throats. This length scale in relation to the dynamic length scale of the flow field could be a parameter describing how the pores are interacting with each other and potentially parameterize the transition of the flow regime from a local instability to a collective phenomenon with global flow field.

It is noteworthy that our geometry, which finds importance in a wide variety of applications in industrial and biological processes, will have significant impact in understanding the onset of fluid turbulence and threshold during polymer extrusion processes, moulding, fluid behaviour in porous media for remediations and local arterial opening during multiple stenosis formation in the prevention of cardiovascular diseases. We also find that our work opens a pathway towards a vast field of research correlating in detail the actual flow field behaviour towards predicting the onset of elastic turbulence.

Supplementary Information The online version contains supplementary material available at <https://doi.org/10.1007/s11242-022-01790-8>.

Acknowledgements The authors gratefully acknowledge the funding of the Shell Digital Rocks Programme.

Author Contributions All authors contributed to the study conception and design. The experiment was designed by EE and PL. The experiments were conducted by EE and the data analysis was performed by EE. The data interpretation was conducted by all authors. The first draft of the manuscript was written by EE, and all authors commented on previous versions of the manuscript and contributed to the final manuscript. All authors read and approved the final manuscript.

Funding Funding of this work was provided by Shell Global Solutions International B.V.

Data Availability The data are included as supplementary information in the form of video files.

Declarations

Conflict of interest E. M. Ekanem was funded by the research grant provided by Shell Global Solutions International B.V. S. Berg and A. Fadili are employed by Shell Global Solutions International B.V. S. De is employed by Shell India Markets Private Limited. Due to the fundamental nature of the work, we believe no competing interests exist.

Open Access This article is licensed under a Creative Commons Attribution 4.0 International License, which permits use, sharing, adaptation, distribution and reproduction in any medium or format, as long as you give appropriate credit to the original author(s) and the source, provide a link to the Creative Commons licence, and indicate if changes were made. The images or other third party material in this article are included in the article's Creative Commons licence, unless indicated otherwise in a credit line to the material. If material is not included in the article's Creative Commons licence and your intended use is not permitted by statutory regulation or exceeds the permitted use, you will need to obtain permission directly from the copyright holder. To view a copy of this licence, visit <http://creativecommons.org/licenses/by/4.0/>.

References

- Alves, M.A., Poole, R.J.: Divergent flow in contractions. *J. Nonnewton. Fluid Mech.* **144**, 140–148 (2007). <https://doi.org/10.1016/j.jnnfm.2007.04.003>
- Browne, C.A., Datta, S.S.: Elastic turbulence generates anomalous flow resistance in porous media. *Sci. Adv.* (2021). <https://doi.org/10.1126/sciadv.abj2619>
- Browne, C.A., Shih, A., Datta, S.S.: Bistability in the unstable flow of polymer solutions through pore constriction arrays. *J. Fluid Mech.* **890**, A2 (2020). <https://doi.org/10.1017/jfm.2020.122>

- Choueiri, G.H., Lopez, J.M., Varshney, A., Sankar, S., Hof, B.: Experimental observation of the origin and structure of elastoinertial turbulence. *Proc. Natl. Acad. Sci. USA.* **118**, e2102350118 (2021). <https://doi.org/10.1073/pnas.2102350118>
- Clarke, A., Howe, A.M., Mitchell, J., Staniland, J., Hawkes, L.A.: How viscoelastic-polymer flooding enhances displacement efficiency. *SPE J.* **21**, 0675–0687 (2016). <https://doi.org/10.2118/174654-PA>
- Cruz, F.A., Poole, R.J., Afonso, A.M., Pinho, F.T., Oliveira, P.J., Alves, M.A.: A new viscoelastic benchmark flow: stationary bifurcation in a cross-slot. *J. Nonnewton. Fluid Mech.* **214**, 57–68 (2014). <https://doi.org/10.1016/j.jnnfm.2014.09.015>
- De, S., Kuipers, J.A.M., Peters, E.A.J.F., Padding, J.T.: Viscoelastic flow past mono- and bidisperse random arrays of cylinders: Flow resistance, topology and normal stress distribution. *Soft Matter* **13**, 9138–9146 (2017a). <https://doi.org/10.1039/c7sm01818e>
- De, S., van der Schaaf, J., Deen, N.G., Kuipers, J.A.M., Peters, E.A.J.F., Padding, J.T.: Lane change in flows through pillared microchannels. *Phys. Fluids.* **29**, 113102 (2017b). <https://doi.org/10.1063/1.4995371>
- De, S., Koesen, S.P., Maitri, R.V., Golombok, M., Padding, J.T., van Santvoort, J.F.M.: Flow of viscoelastic surfactants through porous media. *AIChE J.* **64**, 773–781 (2018a). <https://doi.org/10.1002/aic.15960>
- De, S., Krishnan, P., van der Schaaf, J., Kuipers, J.A.M., Peters, E.A.J.F., Padding, J.T.: Viscoelastic effects on residual oil distribution in flows through pillared microchannels. *J. Colloid Interface Sci.* **510**, 262–271 (2018b). <https://doi.org/10.1016/j.jcis.2017.09.069>
- Ekanem, E.M., Berg, S., De, S., Fadili, A., Bultreys, T., Rücker, M., Southwick, J., Crawshaw, J., Luckham, P.F.: Signature of elastic turbulence of viscoelastic fluid flow in a single pore throat. *Phys. Rev. E* **101**, 42605 (2020). <https://doi.org/10.1103/PhysRevE.101.042605>
- Gao, W., Liu, R., Duan, X., Li, Y.: Numerical investigation on non-Newtonian flows through double constrictions by an unstructured finite volume method. *J. Hydrodyn.* **21**, 622–632 (2009). [https://doi.org/10.1016/S1001-6058\(08\)60193-6](https://doi.org/10.1016/S1001-6058(08)60193-6)
- Garrepally, S., Jouenne, S., Olmsted, P.D., Lequeux, F.: Scission of flexible polymers in contraction flow: predicting the effects of multiple passages. *J. Rheol.* **64**, 601–614 (2020). <https://doi.org/10.1122/1.5127801>
- Groisman, A., Steinberg, V.: Elastic turbulence in a polymer solution flow. *Nature* **405**, 53–55 (2000). <https://doi.org/10.1038/35011019>
- Groisman, A., Steinberg, V.: Elastic turbulence in curvilinear flows of polymer solutions. *New J. Phys.* **6**, 29–29 (2004). <https://doi.org/10.1088/1367-2630/6/1/029>
- Gutiérrez, J.A.F., Moura, M.J.B., Carvalho, M.S.: Dynamics of viscoelastic flow through axisymmetric constricted microcapillary at high elasticity number. *J. Nonnewton. Fluid Mech.* **286**, 104438 (2020). <https://doi.org/10.1016/j.jnnfm.2020.104438>
- Haward, S.J.: Microfluidic extensional rheometry using stagnation point flow. *Biomicrofluidics* **10**, 043401 (2016). <https://doi.org/10.1063/1.4945604>
- Haward, S.J., Kitajima, N., Toda-Peters, K., Takahashi, T., Shen, A.Q.: Flow of wormlike micellar solutions around microfluidic cylinders with high aspect ratio and low blockage ratio. *Soft Matter* **15**, 1927–1941 (2019). <https://doi.org/10.1039/C8SM02099J>
- Haward, S.J., Oliveira, M.S.N., Alves, M.A., McKinley, G.H.: Optimized cross-slot flow geometry for microfluidic extensional rheometry. *Phys. Rev. Lett.* (2012). <https://doi.org/10.1103/PhysRevLett.109.128301>
- Haward, S.J., McKinley, G.H., Shen, A.Q.: Elastic instabilities in planar elongational flow of monodisperse polymer solutions. *Sci. Rep.* **6**, 1–18 (2016). <https://doi.org/10.1038/srep33029>
- Hopkins, C.C., Haward, S.J., Shen, A.Q.: Tristability in viscoelastic flow past side-by-side microcylinders. *Phys. Rev. Lett.* **126**, 054501 (2021). <https://doi.org/10.1103/PhysRevLett.126.054501>
- Hossein, M., Hossein, M., Parvazdavan, M., Morshedi, S.: Experimental investigation of microscopic / macroscopic efficiency of polymer flooding in fractured heavy oil five-spot systems. *J. Energy Resour. Technol.* **135**, 1–9 (2016). <https://doi.org/10.1115/1.4023171>
- Howe, A.M., Clarke, A., Giernalczyk, D.: Flow of concentrated viscoelastic polymer solutions in porous media: effect of M W and concentration on elastic turbulence onset in various geometries. *Soft Matter* **11**, 6419–6431 (2015). <https://doi.org/10.1039/C5SM01042J>
- Jun, Y., Steinberg, V.: Elastic turbulence in a curvilinear channel flow. *Phys. Rev. E* **84**, 56325 (2011)
- Kawale, D., Bouwman, G., Sachdev, S., Zitha, P.L.J., Kreutzer, M.T., Rossen, W.R., Boukany, P.E.: Polymer conformation during flow in porous media. *Soft Matter* **13**, 8745–8755 (2017). <https://doi.org/10.1039/c7sm00817a>
- Khodaparast, S., Borhani, N., Thome, J.R.: Sudden expansions in circular microchannels: Flow dynamics and pressure drop. *Microfluid. Nanofluidics.* (2014). <https://doi.org/10.1007/s10404-013-1321-7>

- Li, J.X., Westerberg, L.G., Höglund, E., Lugt, P.M., Baart, P.: Lubricating grease shear flow and boundary layers in a concentric cylinder configuration. *Tribol. Trans.* **57**, 1106–1115 (2014). <https://doi.org/10.1080/10402004.2014.937886>
- Mahmoodi, H., Fattahi, M., Motevassel, M.: Graphene oxide-chitosan hydrogel for adsorptive removal of diclofenac from aqueous solution: preparation, characterization, kinetic and thermodynamic modelling. *RSC Adv.* **11**, 36289–36304 (2021). <https://doi.org/10.1039/d1ra06069d>
- Mckinley, G.H., Pakdel, P., Oztekin, A., Mckinley, G.H.: Rheological and geometric scaling of purely elastic instabilities. *J. Non-Newtonian Fluid Mech.* **67**, 19–47 (1996)
- Mitchell, J., Lyons, K., Howe, A.M., Clarke, A.: Viscoelastic polymer flows and elastic turbulence in three-dimensional porous structures. *Soft Matter* **12**, 460–468 (2016). <https://doi.org/10.1039/C5SM01749A>
- Mustapha, N., Chakravarty, S., Mandal, P.K., Amin, N.: Unsteady response of blood flow through a couple of irregular arterial constrictions to body acceleration. *J. Mech. Med. Biol.* **8**, 395–420 (2008). <https://doi.org/10.1142/S0219519408002723>
- Pakdel, P., McKinley, G.H.: Elastic instability and curved streamlines. *Phys. Rev. Lett.* **77**, 2459–2462 (1996). <https://doi.org/10.1103/PhysRevLett.77.2459>
- Parsa, S., Santanach-Carreras, E., Xiao, L., Weitz, D.A.: Origin of anomalous polymer-induced fluid displacement in porous media. *Phys. Rev. Fluids.* **5**, 22001 (2020)
- Qi, Q.M., Shaqfeh, E.S.G.: Time-dependent particle migration and margination in the pressure-driven channel flow of blood. *Phys. Rev. Fluids.* **3**, 034302 (2018). <https://doi.org/10.1103/PhysRevFluids.3.034302>
- Qin, B., Salipante, P.F., Hudson, S.D., Arratia, P.E.: Upstream vortex and elastic wave in the viscoelastic flow around a confined cylinder. *J. Fluid Mech.* **864**, 1 (2019)
- Rabby, M.G., Shupti, S.P., Molla, M.M.: Pulsatile non-Newtonian laminar blood flows through arterial double stenoses. *J. Fluids.* **2014**, 1–13 (2014). <https://doi.org/10.1155/2014/757902>
- Raihan, M.K., Jagdale, P.P., Wu, S., Shao, X., Bostwick, J.B., Pan, X., Xuan, X.: Flow of non-newtonian fluids in a single-cavity microchannel. *Micromachines.* (2021). <https://doi.org/10.3390/mi12070836>
- Sadeghi, A., Saïdi, M.H., Veisi, H., Fattahi, M.: Thermally developing electroosmotic flow of power-law fluids in a parallel plate microchannel. *Int. J. Therm. Sci.* **61**, 106–117 (2012)
- Samanta, D., Dubief, Y., Holzner, M., Schäfer, C., Morozov, A.N., Wagner, C., Hof, B.: Elasto-inertial turbulence. *Proc. Natl. Acad. Sci. USA* **110**, 10557–10562 (2013). <https://doi.org/10.1073/pnas.1219666110>
- Skauge, A., Zamani, N., Gausdal Jacobsen, J., Shaker Shiran, B., Al-Shakry, B., Skauge, T.: Polymer flow in porous media: relevance to enhanced oil recovery. *Colloids Interfaces.* **2**, 27 (2018). <https://doi.org/10.3390/colloids2030027>
- Sousa, P.C., Pinho, F.T., Oliveira, M.S.N., Alves, M.A.: Purely elastic flow instabilities in microscale cross-slot devices. *Soft Matter* **11**, 8856–8862 (2015). <https://doi.org/10.1039/C5SM01298H>
- Steinberg, V.: Elastic turbulence: an experimental view on inertialess random flow. *Annu. Rev. Fluid Mech.* **53**, 27–58 (2021). <https://doi.org/10.1146/annurev-fluid-010719-060129>
- van Buel, R., Stark, H.: Active open-loop control of elastic turbulence. *Sci. Rep.* **10**, 1–9 (2020)
- Varshney, A., Steinberg, V.: Elastic Alfvén waves in elastic turbulence. *Nat. Commun.* **10**, 652 (2019). <https://doi.org/10.1038/s41467-019-08551-0>
- Walkama, D.M., Waisbord, N., Guasto, J.S.: Disorder suppresses chaos in viscoelastic flows. *Phys. Rev. Lett.* **124**, 164501 (2019). <https://doi.org/10.1103/PhysRevLett.124.164501>
- Wever, D.A.Z., Picchioni, F., Broekhuis, A.A.: Polymers for enhanced oil recovery: a paradigm for structure-property relationship in aqueous solution. *Prog. Polym. Sci.* **36**, 1558–1628 (2011). <https://doi.org/10.1016/j.progpolymsci.2011.05.006>
- Xie, C., Qi, P., Xu, K., Xu, J., Balhoff, M.T.: Oscillative trapping of a droplet in a converging channel induced by elastic instability. *Phys. Rev. Lett.* **128**, 54502 (2022)
- Yao, G., Zhao, J., Yang, H., Haruna, M.A., Wen, D.: Effects of salinity on the onset of elastic turbulence in swirling flow and curvilinear microchannels. *Phys. Fluids.* **31**, 123106 (2019)
- Zamani, N., Bondino, I., Kaufmann, R., Skauge, A.: Effect of porous media properties on the onset of polymer extensional viscosity. *J. Pet. Sci. Eng.* **133**, 483–495 (2015). <https://doi.org/10.1016/j.petrol.2015.06.025>
- Zhao, Y., Shen, A.Q., Haward, S.J.: Flow of wormlike micellar solutions around confined microfluidic cylinders. *Soft Matter* **12**, 8666–8681 (2016). <https://doi.org/10.1039/C6SM01597B>
- Zilz, J., Poole, R.J., Alves, M.A., Bartolo, D., Levaché, B., Lindner, A.: Geometric scaling of a purely elastic flow instability in serpentine channels. *J. Fluid Mech.* **712**, 203–218 (2012). <https://doi.org/10.1017/jfm.2012.411>

Zografos, K., Hartt, W., Hamersky, M., Oliveira, M.S.N., Alves, M.A., Poole, R.J.: Viscoelastic fluid flow simulations in the e-VROCTM geometry. *J. Nonnewton. Fluid Mech.* **278**, 104222 (2020). <https://doi.org/10.1016/j.jnnfm.2019.104222>

Publisher's Note Springer Nature remains neutral with regard to jurisdictional claims in published maps and institutional affiliations.

Authors and Affiliations

Eseosa M. Ekanem¹ · Steffen Berg^{1,2}  · Shauvik De³ · Ali Fadili² · Paul Luckham¹

✉ Steffen Berg
steffen.berg@shell.com

¹ Department of Chemical Engineering, Imperial College London, London SW7 2AZ, UK

² Shell Global Solutions International B.V, Grasweg 31, 1031HW Amsterdam, The Netherlands

³ Shell India Markets Private Limited, Bangalore, Karnataka 562149, India